C. R. Mecanique 342 (2014) 156–173

Contents lists available at ScienceDirect

Comptes Rendus Mecanique

www.sciencedirect.com

Micromechanics of granular materials – A tribute to Ching S. Chang

Analysis of local behaviour in granular materials

Analyse du comportement local des matériaux à une échelle mésoscopique

Ngoc-Son Nguyen, Hélène Magoariec *, Bernard Cambou

LTDS – UMR 5513, École centrale de Lyon, 36, avenue Guy-de-Collongue, 69134 Écully cedex, France

ARTICLE INFO

Article history:
Available online 14 March 2014

Keywords:
Granular material
Multi-scale approach
Discrete element method
Meso-scale
Local behaviour

Mots-clés :
Matériaux granulaires
Approche multi-échelles
Méthode des éléments discrets
Échelle mésoscopique
Comportement local

ABSTRACT

A local scale, called the *meso-scale*, has recently been introduced to the multi-scale approach for 2D granular materials. This local scale is defined at the level of meso-domains enclosed by particles in contact. Stress and strain have been defined at this local scale, and their relation with the local structure has been studied. The purpose of this paper is to analyse the behaviour of granular materials at the meso-scale, i.e. the stress–strain–structure relationship at this scale. Analyses are performed on a 2D numerical granular sample subjected to a biaxial compression test and simulated with the Discrete Element Method (DEM). The sample is quite dense and it is loaded at a relatively low strain rate so that the state of the sample can be considered as being quasi-static. The size of sub-domains in the sample varies largely from 3 to 12 particles. It is shown that the evolution of the internal state of the sample corresponds, at the meso-scale, to a clear evolution of the quantity of meso-domains oriented in different directions. In addition, the behaviour of meso-domains is highly governed by their orientation rather than their density, especially for the strongly elongated meso-domains: the meso-domains oriented in the compression (resp. extension) direction behave like a dense (resp. loose) granular material.

© 2014 Published by Elsevier Masson SAS on behalf of Académie des sciences.

RÉSUMÉ

Une échelle locale, appelée *l'échelle mésoscopique*, a été introduite récemment dans l'approche multi-échelles pour les matériaux granulaires 2D. Cette échelle est définie au niveau de sous domaines constitués de boucles fermées limitées par des particules en contacts. La contrainte et la déformation ont été définies à cette échelle, et leur relation avec la structure locale a été étudiée. L'objectif de cet article est d'analyser le comportement local des milieux granulaires à cette échelle, c'est-à-dire la relation entre contrainte, déformation et structure. Des analyses sont réalisées sur la simulation numérique, par la méthode des éléments discrets, d'un essai de compression biaxiale d'un échantillon de matériau granulaire 2D. L'échantillon considéré est relativement dense et la sollicitation est suffisamment lente pour que l'échantillon puisse être considéré dans un régime quasi statique. Le nombre de particules dans chaque sous-domaine varie de 3 à 12. Les analyses réalisées montrent que l'évolution de l'état interne de l'échantillon correspond à une évolution de la quantitié des sous-domaines orientés dans des directions différentes. De plus, le comportement des sous-domaines est fortement piloté par leur

* Corresponding author.
E-mail addresses: ngocson.nguyen@bwk.kuleuven.be (N.-S. Nguyen), helene.magoariec@ec-lyon.fr (H. Magoariec), bernard.cambou@ec-lyon.fr (B. Cambou).

http://dx.doi.org/10.1016/j.crme.2014.01.004
1631-0721/© 2014 Published by Elsevier Masson SAS on behalf of Académie des sciences.

orientation, plutôt que par leur densité. Les sous-domaines orientés dans la direction de compression se comportent comme un matériau dense, tandis que ceux orientés dans la direction d'extension se comportent comme un matériau lâche.
© 2014 Published by Elsevier Masson SAS on behalf of Académie des sciences.

1. Introduction

The behaviour of granular materials is quite complex and the phenomenological models available in the literature are not able to give accurate forecasts for complex loading such as cyclic loadings or loadings with rotation of principal stress directions. Furthermore, these phenomenological models consider a large set of constants which are often difficult to identify from experimental tests and which may have unclear physical meanings. To overcome these difficulties, many authors have proposed to develop a multi-scale approach, which has the main advantage of taking into account phenomena occurring at a local level [1–6]. Thus the macroscopic laws derived from local structural and mechanical information are expected to be more efficient than the afore-mentioned phenomenological laws. Two important multi-scale approaches have been proposed in the literature. The first approach [1,2,7–9] considers a local scale, called *micro-scale*, defined at the level of contacts between particles. At this scale, the local static variables are the interparticle contact forces, which can easily be related to the static variable at the macro-scale defined at the representative elementary volume (REV): the stress tensor. However, it is more difficult to relate the kinematic variables defined at contacts (relative displacements at contacts) directly to the macroscopic kinematic variable, the strain tensor, as proved by various authors [10,11]. Thus, this kind of approach can only provide approximations of the behaviour of granular materials in the domain of very small strain, which can be considered as the elastic domain. The second approach [6] considers, at the micro-scale, a local behaviour law similar to classical global phenomenological behaviour laws for granular materials. Thus, this approach can be considered as a mixture between a multi-scale approach and a phenomenological approach. This approach is interesting because it allows microscopic properties to be added to a phenomenological approach; however, it has some of the same drawbacks as the usual phenomenological approaches mentioned above. In order to overcome these difficulties when considering the micro-scale, some multi-scale approaches have introduced or suggested an intermediate scale between the micro-scale and macro-scale, which is defined at the level of clusters of particles [3,4,12–16]. Such an intermediate local scale is expected to allow the local structure of granular materials to be more precisely described and the local static and kinematic variables to be more consistently defined. In two previous papers [17,18], an intermediate local scale, called *the meso-scale*, has been defined for 2D granular materials. Using the particle graph proposed in [12], a 2D granular material is entirely subdivided into meso-domains, each of which is enclosed by branches which unite the centres of the particles in contact. The meso-scale is then defined at the level of these meso-domains. In these papers, the meso-structure has been described, and meso-stress and meso-strain have been consistently defined and analysed. It has been shown that the meso-stress and meso-strain fields are significantly structured, i.e. meso-stress and meso-strain are significantly governed by the meso-domain elongation degree and orientation. This paper is a continuation of these works, and its main purpose is to analyse the behaviour of granular materials at the meso-scale. More specifically, the stress–strain–structure relationship at the meso-scale will be analysed in detail.

In Section 2, we describe the numerical simulation of a granular sample subjected to a biaxial compression test. The meso-scale considered in this paper is defined, and the structure at this scale is briefly analysed in the same section. Sections 3 and 4 recall the stress and strain definitions at the meso-scale and briefly present some important results concerning the local stress and strain fields. Section 5 focuses on analysing the behaviour of the granular sample simulated at the meso-scale.

2. Definition and characterization of the meso-scale

2.1. Description of the biaxial test

The analyses presented in this paper have been carried out through a numerical biaxial test simulated with software PFC^{2D} (Particle Flow Code), which is identical to that considered in our two previous papers [17,18]. This piece of software is developed and licensed by HCItasca and based on the work initiated by Cundall [19]. In this method, particles are assumed to be rigid and a small local overlap is allowed at each contact. This overlap is related to the contact force by a contact law using normal and tangential springs. Furthermore this contact law considers the Coulomb's friction law. The system of equations—Newton's dynamical equation and the force–overlap relation at the contact points—is numerically solved by a time-stepping algorithm as described in [20]. The numerical sample is composed of 25,000 disks (2D analysis) that are randomly generated in a rectangular box with four frictionless rigid walls. The sample is 1.35 m high and 0.9 m wide. The diameter of the disks is uniformly distributed from 4.8 mm to 9.6 mm with a mean value equal to 7.2 mm. For the contact law, linear springs are considered with the normal and tangential stiffnesses equal to 5.0×10^7 N/m, and Coulomb's friction angle is equal to 30°. The chosen value for the normal stiffness is not very high, which may result in a relatively high overlap between particles. However, this value allows us to keep the simulation time reasonable. The step size used for

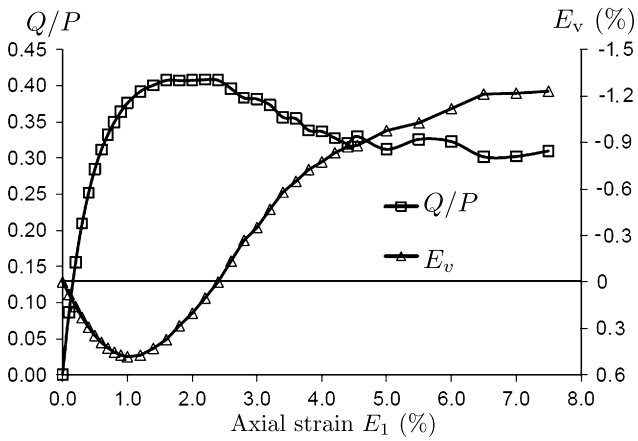

Fig. 1. Evolutions of the stress ratio Q/P and of the volumetric strain E_v of the sample during the biaxial test.

the simulation is automatically selected by the computer program, depending on the mass of particles, the stiffness of the contacts, the number of contacts, etc., and its order of magnitude is 10^{-5} s. It should be noted that a 2D sample of disks is equivalent to a 3D sample composed of cylinders that are 1 m long. The sample is then compacted isotropically [17] until an isotropic stress state of 100 kPa is reach. At the end of the compaction process, the sample is almost isotropic and quite dense, with a porosity equal to 0.16 and a coordination number equal to about 3.8. The biaxial test is performed by slowly compressing the sample in the vertical direction (denoted as direction (1)) with a strain rate $\dot{E}_1 = -10^{-2}$ 1/s, while keeping a constant stress $\Sigma_2 = 100$ kPa in the perpendicular direction, i.e. the horizontal direction, (denoted as direction (2)). In the following, we simply call direction (1) as the *compression direction* and direction (2) as the *extension direction*.

In Fig. 1, we can observe that under the biaxial test the granular sample shows the classical behaviour of a quite dense granular medium. The sample first contracts until an axial strain $E_1 \approx 1\%$ (the characteristic strain) and then dilates. The value of 1% obtained for the characteristic strain is slightly higher than the value shown in the literature, which results from the relatively low value chosen for the normal stiffness, leading to a non-negligible elastic deformation at the beginning of the loading. The stress state of the sample is represented by the stress ratio Q/P with P and Q being respectively the mean and deviator stresses defined as follows:

$$P = \frac{\Sigma_{ii}}{2}, \qquad Q = \sqrt{\frac{\Sigma^{\mathrm{d}}_{ij}\Sigma^{\mathrm{d}}_{ij}}{2}} \tag{1}$$

where $\boldsymbol{\Sigma}^{\mathrm{d}}$ is the deviatoric part of the stress tensor $\boldsymbol{\Sigma}$ ($\boldsymbol{\Sigma}^{\mathrm{d}} = \boldsymbol{\Sigma} - P\boldsymbol{I}$). In the present biaxial test, the stress tensor $\boldsymbol{\Sigma}$ is diagonal, with Σ_1 and Σ_2 being respectively the major and minor principal stresses, so we can write:

$$P = \frac{\Sigma_1 + \Sigma_2}{2}, \qquad Q = \frac{\Sigma_1 - \Sigma_2}{2} \tag{2}$$

As shown in Fig. 1, the stress ratio Q/P of the sample first increases, reaches a peak at $E_1 \approx 2\%$ (this state is called *the peak state*), then decreases slightly and finally becomes constant when the volumetric strain also becomes constant (critical state).

It has been observed in [17] that some shear bands appear in the sample when the loading is close to the peak state. The strain is highly spatially organized in such shear bands. These shear bands make the local strain in the sample more complex to analyse. This is the reason why, in the following, the local strain is only analysed until 2% of the axial strain E_1, which is prior to the peak state. Nevertheless, other local variables such as the local structure and the local stress might be not spatially organized, so they can be analysed until 5% or 6% of the axial strain E_1.

2.2. Definition of the meso-scale

As mentioned in the introduction, the meso-scale considered in this paper is defined at the level of meso-domains obtained from Satake's partition of a 2D granular material [12]. For this partition, the author introduced the so-called particle graph that is composed of *closed branches*, each of which connects two particles in contact. The set of closed branches entirely subdivides the medium into meso-domains, each of which corresponds to a set of particles that constitutes a closed loop and surrounds a local void volume in the medium as illustrated in Fig. 2. Therefore the meso-domains are also called *void-cells*. The particle graph was also considered in other approaches [13,14,21,22], in which the local structure and the local strain at the level of meso-domains are investigated. It is worth mentioning that such a meso-scale has so far only been defined for 2D granular materials. Extension to 3D media is not straightforward, due to the complexity of 3D granular structures, and constitutes a challenge for future research.

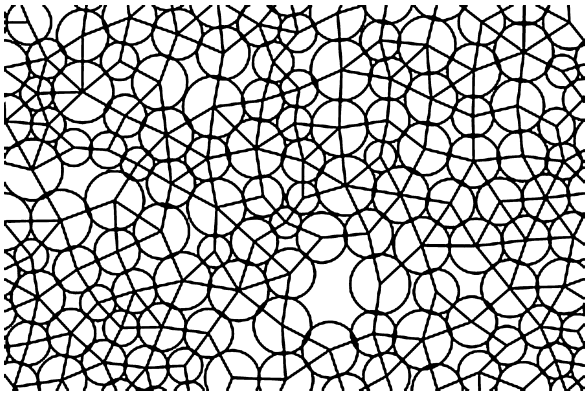

Fig. 2. Part of the granular assembly at the initial state subdivided into meso-domains by means of the particle graph.

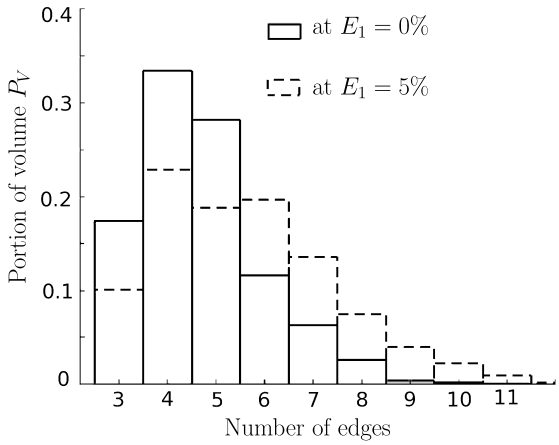

Fig. 3. Amount of volume occupied by the meso-domains with respect to their number of edges.

The construction of the particle graph for an assembly of disks was described in detail in [17]. In this construction, all the *idle particles*, i.e. particles having no contact or only one contact, are excluded from the particle graph because they do not take any part in supporting the loading. However, during loading an idle particle may be activated and takes part in the particle graph. Furthermore, the contact network in the material evolves considerably so the particle graph must be updated throughout the loading.

For the granular sample of 25,000 disks considered in this paper, the particle graph at the initial state contains 23,056 load-bearing particles (after eliminating all the idle particles), 45,855 closed branches and 22,800 meso-domains whose number of edges varies widely from 3 to 12 with a mean value of 4.0 edges per meso-domain. Fig. 3 presents the composition of the particle graph built at the initial state and at axial strain level $E_1 = 5\%$ in terms of amount of volume P_V occupied by meso-domains with the same number of edges. It is shown that meso-domains with a low number of edges (3, 4, 5 edges) are the most present in the particle graph at the initial state. During loading, there is a gradual loss of these meso-domains and a gradual creation of meso-domains with a higher number of edges (6, 7, 8 edges). This means that the meso-domains in the particle graph tend to increase their number of edges during loading. The increase in number of edges per meso-domain certainly results from the gradual loss of contacts in the sample during the biaxial test and can be related to the dilatancy which occurs at large strains.

2.3. Structure at the meso-scale

2.3.1. Description of the structure at the meso-scale

Each meso-domain in the particle graph is composed of a central void enclosed by particles in contact. Therefore, the structure of a meso-domain is essentially defined by the density and texture of the arrangement of particles in the considered meso-domain. In this section, we briefly describe the meso-domain structure (see [17,18,21,22] for more details).

The density of a meso-domain is described by two variables: porosity po^h, defined as the ratio of the void volume inside the meso-domain to the volume of the meso-domain, and valence r^h, defined as the number of contacts of the meso-domain. Note that the idle particles are excluded when computing porosity po^h.

The texture of a given meso-domain is described by a loop tensor defined as:

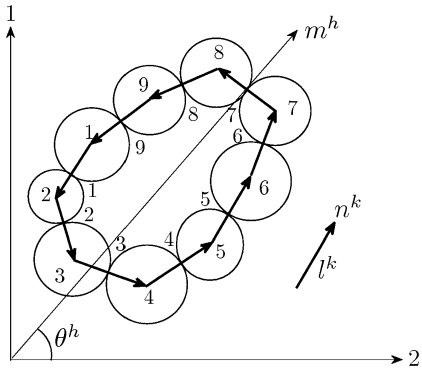

Fig. 4. Illustration of a meso-domain composed of closed branches, each of which has a length l^k and a direction given by a unit vector $\boldsymbol{n}^k$. The elongation direction $\boldsymbol{m}^h$ of the meso-domain forms an angle θ^h with respect to the extension direction 2.

$$\boldsymbol{L}^h = \sum_{k=1}^{r^h} l^k \boldsymbol{n}^k \otimes \boldsymbol{n}^k \tag{3}$$

where $\boldsymbol{n}^k$ is a unit vector directing branch k of length l_k (Fig. 4), and the dyadic product ($\otimes$) for two vectors is defined as $\boldsymbol{a} \otimes \boldsymbol{b} = a_i b_j$. The loop tensor (3) is obtained by modifying the loop tensor proposed in [21] in such a way that its trace is equal to the perimeter of the meso-domain under consideration. We can see that the loop tensor $\boldsymbol{L}^h$ defined by Eq. (3) includes not only orientation $\boldsymbol{n}^k$ but also the length l^k of the branches of each meso-domain. Therefore, the loop tensor $\boldsymbol{L}^h$ is a measure of the size, shape and orientation of each meso-domain. We proposed in [17] to describe the texture of a meso-domain by two parameters defined from the loop tensor $\boldsymbol{L}^h$ as follows:

- its elongation degree β^h:

$$\beta^h = \frac{\sqrt{D^h_{ij} D^h_{ij}}}{L^h_{kk}} \tag{4}$$

  where $\boldsymbol{D}^h$ is the deviatoric part of $\boldsymbol{L}^h$. A high value of β^h means that the meso-domain under consideration is highly elongated;
- the major principal direction of $\boldsymbol{L}^h$ corresponds to the elongation direction $\boldsymbol{m}^h$ of the meso-domain under consideration, which defines geometrically its maximum dimension as illustrated in Fig. 4. The orientation angle θ^h of each meso-domain is defined as the angle between the elongation direction $\boldsymbol{m}^h$ and the extension direction (2) (see Fig. 4).

It is worth mentioning that the elongation degree β^h defined in this approach for each meso-domain is quite similar to a measure called "anisotropy-index" proposed in [21], which is defined as the inner product of the deviatoric part of $\boldsymbol{D}^h$. The only difference between these two measures is that for the elongation degree β^h the inner product of $\boldsymbol{D}^h$ is normalized by the trace of the loop tensor $\boldsymbol{L}^h$, which is considered as the size of each meso-domain. Fig. 5 illustrates six meso-domains with different elongation degree β^h and elongation direction $\boldsymbol{m}^h$. As can be seen in Fig. 6, the meso-domain elongation degree β^h is highly heterogeneous: it varies largely from $\beta_{\min} \approx 0$ to $\beta_{\max} \approx 0.5$ with a volume-weighted mean value $\langle\beta\rangle_{\mathrm{v}} \approx 0.2$. In addition, the distribution of the meso-domain elongation degree β^h remains approximately unchanged during loading [18]. In order to analyse simply the role of the elongation degree β^h and the orientation θ^h of the meso-domains in the sample, we define six meso-domain types as shown in Table 1. For this purpose, all the meso-domains in the sample are first split, according to the elongation degree β^h, into class W containing the *weakly* elongated meso-domains (with a value of β^h lower than the mean value) and class S containing the *strongly* elongated meso-domains (with a value of β^h higher than the mean value). Next, the meso-domains in each class are split, according to the orientation angle θ^h, into three sub-classes C, I, E containing the meso-domains oriented in the *compression*, *intermediate* and *extension* directions. In this way, we obtain six meso-domain types SC, SI, SE, WC, WI, WE, which differ from each other in the elongation degree and orientation. These six-domain types can be thought of as being six local phases of the sample, and their structure can represent the local structure of the sample. In the following, the evolution of the structure of the six phases during the biaxial test will be analysed.

It is worth mentioning that the analysis presented in this paper, in which different phases of meso-domains with different orientations and elongation degrees are pointed out, has some common points with the microplane approach developed in particular by Bazant et al. [23]. Nevertheless, these two approaches are quite different. In the microplane approach, the local strain has, as a first step, to be defined in the local axes linked to different local planes. This is not the case in the analysis presented in this paper.

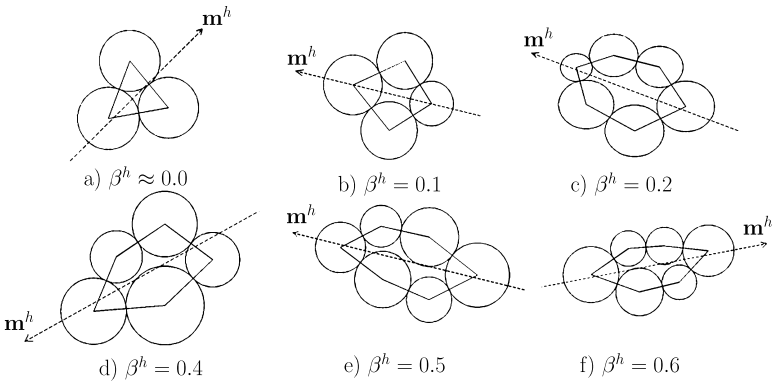

Fig. 5. Illustration of six sub-domains with different elongation degrees β^h and orientations $\boldsymbol{m}^h$.

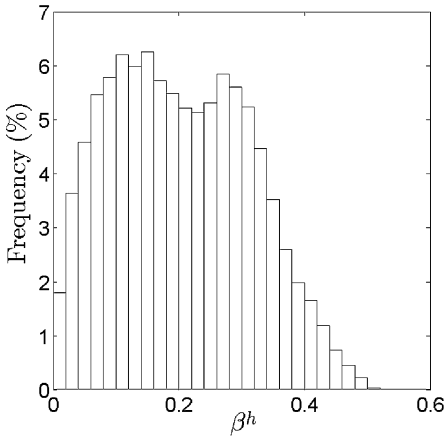

Fig. 6. Distribution of the elongation degree β^h of meso-domains at the loading level $E_1 = 1.2\%$. The ordinate represents the percentage (in number) of the meso-domains corresponding to each bar.

Table 1
Classification of all the meso-domains into two classes W and S, and six meso-domain types WC, WI, WE, SC, SI, SE.

Classes	Meso-domain types	Elongation degree β^h	Orientation angle θ^h
W	WC	$[\beta_{\min}, \langle\beta\rangle_{\mathrm{v}}]$	$[60°, 120°]$
	WI		$[30°, 60°] \cup [120°, 150°]$
	WE		$[0, 30°] \cup [150°, 180°]$
S	SC	$[\langle\beta\rangle_{\mathrm{v}}, \beta_{\max}]$	$[60°, 120°]$
	SI		$[30°, 60°] \cup [120°, 150°]$
	SE		$[0, 30°] \cup [150°, 180°]$

2.3.2. Evolution of the structure at the meso-scale

a) Amount of volume of the phases

It has been shown in [17,18,22] that the meso-domains are isotropically oriented at the initial state. During deviatoric loading, new meso-domains oriented in the compression direction are created and meso-domains oriented in the extension direction are destroyed. This evolution results from the creation of contacts oriented in the compression direction and the loss of contacts oriented in the extension direction. As a result, meso-domains evolve dynamically throughout the loading: some new meso-domains are created and some meso-domains are destroyed in the sample. These creation and destruction of meso-domains lead to a change in the amount of volume P_{V} of the six phases SC, SI, SE, WC, WI, WE (P_{V} is the ratio of the total volume of all the meso-domains in each phase to the volume of the sample) during loading, as shown in Fig. 7. Due to the isotropy of the initial state, the amount of volume P_{V}, at this state, is approximately the same for all the phases. We can see that the phases change volume greatly during loading depending on their orientation, in particular for the strongly elongated phases (SC, SI, SE). During loading, the amount of volume P_{V} of phase SC increases quickly, reaches a maximum value at the peak state, and then decreases slightly, whereas the amount of volume P_{V} of phase SE decreases

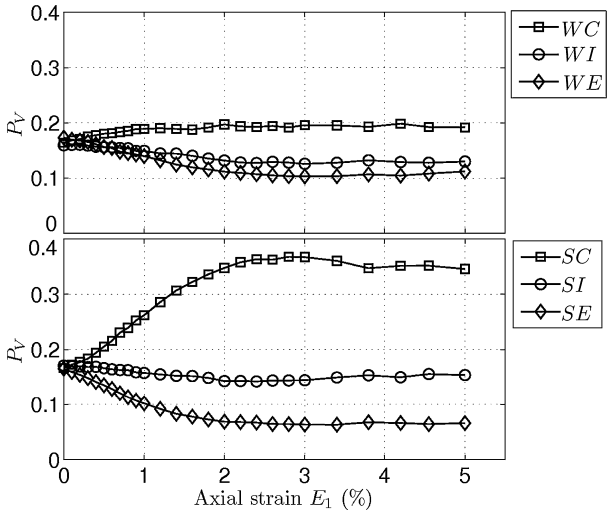

Fig. 7. Evolution of the amount of volume P_V of the six phases WC, WI, WE, SC, SI, SE during loading.

quickly, reaches the minimum value at the peak state, and then remains approximately constant. The phase SI occupies a fairly constant volume during loading. This change in volume of the six phases reflects the evolution of the anisotropy of the granular sample observed at the meso-scale.

b) Contribution of the phases to the global anisotropy

In order to characterize the texture of the sample in terms of the orientation of the meso-domains, we define a texture tensor as follows:

$$\boldsymbol{T} = \frac{1}{V}\sum_{h=1}^{N_h} V^h \boldsymbol{m}^h \otimes \boldsymbol{m}^h \tag{5}$$

where V^h and V are, respectively, the volumes of each meso-domain and of the sample, $\boldsymbol{m}^h$ is the elongation direction of each meso-domain, and N^h is the total number of meso-domains in the sample. Similarly, we define a texture tensor for each phase, for example tensor $\boldsymbol{T}^{SC}$ for phase SC, as follows:

$$\boldsymbol{T}^{SC} = \frac{1}{V}\sum_{h\in SC} V^h \boldsymbol{m}^h \otimes \boldsymbol{m}^h \tag{6}$$

where the sum covers all the meso-domains in each phase (SC, for example). One can see that: $\boldsymbol{T} = \boldsymbol{T}^{SC} + \boldsymbol{T}^{SI} + \boldsymbol{T}^{SE} + \boldsymbol{T}^{WC} + \boldsymbol{T}^{WI} + \boldsymbol{T}^{WE}$. Therefore, the texture tensor for each phase ($\boldsymbol{T}^{SC}$, for example) can be understood as the contribution of each phase (SC, for example) to the global texture. The computation of the above texture tensors shows that they are approximately diagonal. Therefore, we can characterize the level of anisotropy of the sample by a measurement:

$$T_\mathrm{d} = T_{11} - T_{22} \tag{7}$$

where T_{11} and T_{22} are the components of the texture tensor $\boldsymbol{T}$ in the compression direction (1) and the extension direction (2), respectively. Similarly, the contribution of each phase (phase SC, for example) to the global anisotropy is quantified by $T_\mathrm{d}^{SC} = T_{11}^{SC} - T_{22}^{SC}$. We can obtain $T_\mathrm{d} = T_\mathrm{d}^{SC} + T_\mathrm{d}^{SI} + T_\mathrm{d}^{SE} + T_\mathrm{d}^{WC} + T_\mathrm{d}^{WI} + T_\mathrm{d}^{WE}$. It should be noted that tensor $\boldsymbol{T}$ is approximately diagonal for a biaxial compression test so T_d characterizes the deviatoric part of $\boldsymbol{T}$. Therefore, a zero value of T_d means that the sample is isotropic, and a high value of T_d means that the sample is highly anisotropic. Fig. 8 shows the evolution of the contributions of the six phases to the global anisotropy during loading, compared to the evolution of the global anisotropy T_d divided by 6 (case of equal contributions of the six phases to the global anisotropy). We can see that, at the initial state where the sample is isotropic, the anisotropy of the considered phases depends on their orientation with $T_\mathrm{d}^{SC} \approx T_\mathrm{d}^{WC} \approx -T_\mathrm{d}^{SE} \approx -T_\mathrm{d}^{WE}$. During loading the global anisotropy T_d increases, which confirms that the meso-domains are more and more preferentially oriented in the compression direction. Moreover, phases SC, SE, and WE show a greater contribution to the evolution of the global anisotropy of the sample, in particular phase SC.

c) Density of the phases

We have previously analysed how the six phases change volume and contribute to the global anisotropy during the biaxial test. In the following, the analysis is focused on how the phases change density during loading. Fig. 9 shows the

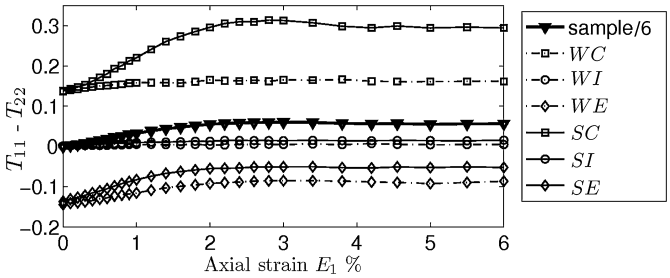

Fig. 8. Evolution of the anisotropy level $T_d = T_{11} - T_{22}$ of the six phases WC, WI, WE, SC, SI, SE during loading.

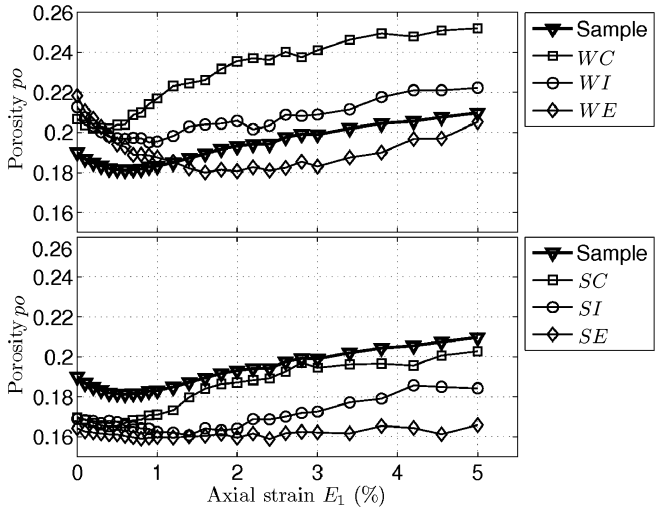

Fig. 9. Evolution of mean porosity po of the six phases WC, WI, WE, SC, SI, SE during loading, compared to that of the sample.

evolution of the mean porosity po of the six phases during loading (po is the volume-weighted mean value of po^h over all the meso-domains in each phase). We can observe a high heterogeneity in density inside the sample even at the initial state, despite the fact that the sample is initially compacted to be as homogeneous as possible. At the initial state, the weakly elongated phases (WC, WI, WE) are looser than the sample, whereas the strongly elongated phases (SC, SI, SE) are denser than the sample. In addition, the porosity of the phases appears to be independent of their orientation at this state, which reflects the isotropy of the sample. However, during deviatoric loading, the density of the phases evolves differently in a way which depends significantly on their orientation. Phase WC (resp. SC) becomes much looser than phase WI (resp. SI) which becomes, in its turn, much looser than phase WE (resp. SE). Moreover, the density of the weakly elongated phases (WC, WI, WE) is more highly dependent on their orientation than that of the strongly elongated phases (SC, SI, SE). We can remark that phase WE follows such a long compaction process that it becomes denser than the sample, while the porosity of phase SE remains approximately constant during loading. Throughout the loading, the porosity of the strongly elongated phases remains lower than that of the sample, whereas the porosity of the weakly elongated phases remains higher than that of the sample, except for phase WE.

Fig. 10 shows the evolution of mean valence r of the six phases during loading. On the whole, mean valence r of the strongly elongated phases (SC, SI, SE) is higher than the mean value R defined for the whole sample, whereas mean valence r of the weakly elongated phases (WC, WI, WE) is lower than R. Like the mean porosity, mean valence r is independent of the orientation of the phases at the initial state. During deviatoric loading, mean valence r of the six phases increases, in particular for the phases oriented in the compression direction (SC and WC). Mean valence r of phase SC (resp. WC) is the highest, whereas mean valence r of phase SE (resp. WE) is the lowest. Phase SI (resp. WI) has an intermediate mean valence between phases SC and SE (resp. WC and WE).

The above analyses show that considering the meso-scale allows one to have an interesting and more comprehensive description of the local structure of 2D granular media. The local structure of the material is composed of many closed sub-structures (meso-domains) with different densities, orientations and elongation degrees. In a simple way, the material can be thought of as being made up of the six local phases SC, SI, SE, WC, WI, WE which correspond to two strong and weak elongation degrees and three orientations in the compression, intermediate and extension directions, respectively. We have shown that the evolution of the internal state of the granular material during the biaxial test results in the evolution of the volumes occupied by these six phases.

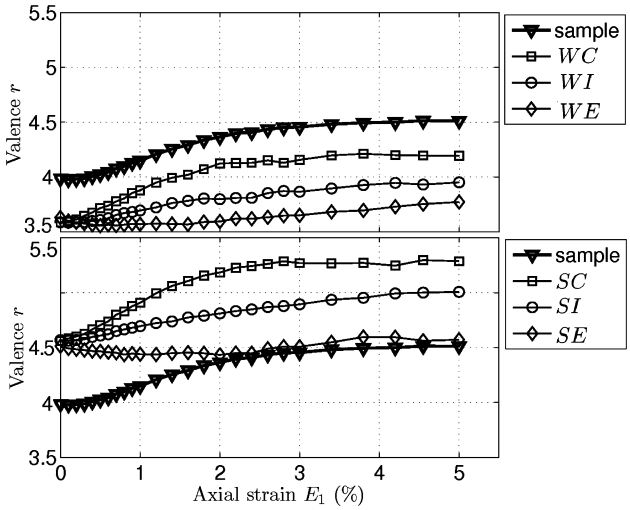

Fig. 10. Evolution of mean valence r of the six phases WC, WI, WE, SC, SI, SE during loading, compared to mean valence R of the whole sample.

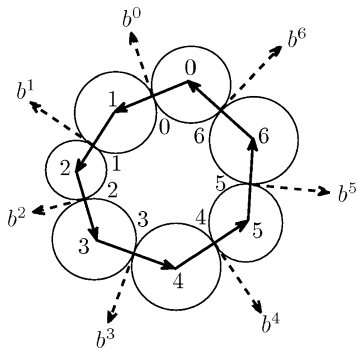

Fig. 11. Local variables considered in Kuhn's strain definition.

3. Strain at the meso-scale

Different approaches have been proposed to define a local strain tensor within a meso-domain. In Kruyt and Rothenburg's approach [13], the displacement field is assumed to be linear along each edge of the meso-domain under consideration. Another approach consists in first defining a local strain tensor within each triangle connecting three neighbouring particles, then taking the volume-weighted mean strain over all the triangles obtained by a triangulation of the meso-domain under consideration. The strain tensor within each triangle can be defined by the approaches of Bagi [24] and of Cambou et al. [10]. Bagi has made the same assumption for each triangle as Kruyt and Rothenburg, while Cambou et al. have assumed a constant strain within each triangle. It is worth noting that all the assumptions mentioned above are equivalent. Kuhn [14] has adapted this method to formulate a local strain tensor $\delta\boldsymbol{\varepsilon}^h$ within a given meso-domain h as follows:

$$\delta\boldsymbol{\varepsilon}^h = \frac{1}{6V^h} \sum_{j_1, j_2 \in \{0,1,\ldots,r^h-1\}} \boldsymbol{Q}^{r^h}_{j_1,j_2} \delta\boldsymbol{u}^{j_1} \otimes^s \boldsymbol{b}^{j_2} \tag{8}$$

where:

- $\delta\boldsymbol{u}^{j_1}$ is the relative displacement between two centres of particles in contact j_1: $\delta\boldsymbol{u}^{j_1} = \delta\boldsymbol{u}^{j_1,m} - \delta\boldsymbol{u}^{j_1,n}$ with $\delta\boldsymbol{u}^{j_1,m}$ and $\delta\boldsymbol{u}^{j_1,n}$ being respectively the translation of the first particle $m = j_1$ and of the second particle $m = j_1 + 1$ at the contact (see Fig. 11);
- $\boldsymbol{b}^{j_2}$ is an outward normal vector to edge j_2 with a magnitude equal to the length of edge j_2;
- symmetrized dyadic product $\otimes^s$ is defined as: $\boldsymbol{a} \otimes^s \boldsymbol{b} = (a_i b_j + b_i a_j)/2$;
- $\boldsymbol{Q}^{r^h}_{j_1,j_2}$ is a skew symmetric and square matrix of dimension $r^h \times r^h$ which is defined in detail in [14,22];
- V^h is the volume of the considered meso-domain.

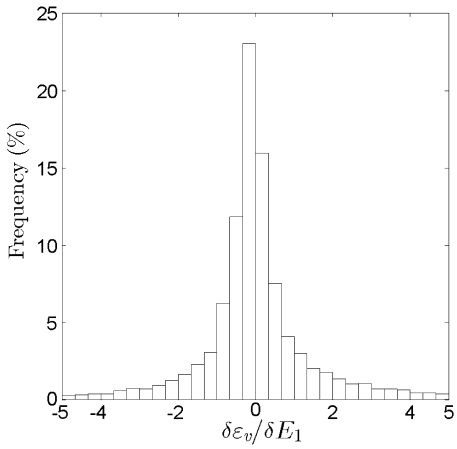

Fig. 12. Distribution of the volumetric strain $\delta\varepsilon_v$ of meso-domains, normalized by the macroscopic axial strain δE_1, at the loading level $E_1 = 1.2\%$.

In fact, the definitions of Kruyt and Rothenburg [13] and of Kuhn [14] differ from each other in the way of formulating the meso-strain tensor $\delta\boldsymbol{\varepsilon}^h$; however they give identical results. It is important to note that definition (8) must be used for a small increment of loading, due to the fact that a meso-domain can be created or destroyed at any moment during loading. In this paper, the meso-strain field $\delta\boldsymbol{\varepsilon}^h$ is computed for increments of loading that correspond to a change in the axial strain $\delta E_1 = 0.02\%$ at the level of the sample. Throughout the present paper, the strain must be understood in the incremental sense, i.e. strain is defined for a given increment of loading. The global strain $\delta\boldsymbol{E}$ is estimated as the volume-weighted mean strain over all the meso-domains in the sample. It has been shown that the global strain $\delta\boldsymbol{E}$ defined by the approaches mentioned above is very close to the strain defined by the boundary condition [11,17]. As mentioned previously, the global strain cannot be well estimated from the relative displacement between two centres of particles in contact and the local geometry at the contact points (at the micro-scale). However, when the meso-scale is considered as a bridge between the micro- and macro-scales, the global strain can be well estimated from the latter local kinematic variable *in addition to the local geometry at the meso-scale* (characterized by the set of vectors $\boldsymbol{b}^{j_2}$ illustrated in Fig. 11). This constitutes another advantage of the meso-scale.

The meso-strain field $\delta\boldsymbol{\varepsilon}^h$ defined in Eq. (8) has been analysed in detail in [17,22]. It has been shown that the meso-strain field $\delta\boldsymbol{\varepsilon}^h$ is very heterogeneous. Fig. 12 shows the dispersion of the volumetric strain $\delta\varepsilon_v$ of meso-domains at the loading level $E_1 = 1.2\%$, at which the volumetric strain δE_v of the sample is almost zero. It can be seen that meso-domains deform differently from each other and from the sample: some meso-domains are strongly dilating, while other meso-domains are strongly contracting.

In this paper, we analyse briefly the local strain within the six phases SC, SI, SE, WC, WI, WE defined in Section 2.3. The local strain tensor $\delta\boldsymbol{\varepsilon}$ in each phase is defined as the volume-weighted average of local strain tensors $\delta\boldsymbol{\varepsilon}^h$ over all the meso-domains in the considered phase. For all the six phases, the mean strain tensor $\delta\boldsymbol{\varepsilon}$ is found to be approximately diagonal in the loading part prior to the peak state. This means that the principal directions of the local strain within the phases coincide approximately with the respective macroscopic ones. The dilatancy of each phase is characterized by a strain ratio, denoted as R_ε:

$$R_\varepsilon = \frac{\delta\varepsilon_{11} + \delta\varepsilon_{22}}{\delta\varepsilon_{22} - \delta\varepsilon_{11}} \tag{9}$$

where $\delta\varepsilon_{11}$ and $\delta\varepsilon_{22}$ are the strain components of the phase under consideration in the principal directions (1) and (2) of the macroscopic stress, respectively. When $R_\varepsilon < 0$ (resp. $R_\varepsilon > 0$), the phase under consideration contracts (resp. dilates). Fig. 13 shows the evolution of the strain ratio R_ε of the six phases during loading. We can see that the local strain within the six phases evolves differently from the macroscopic strain in a way significantly dependent on phase orientation, in particular for the strongly elongated phases (SC, SI, SE). This dependence can be more clearly observed when the local deviatoric loading is high. Phase SC dilates greatly like a dense material, whereas phase SH contracts throughout the loading like a loose material. Phase SI behaves like a material having an intermediate density, moreover its volumetric behaviour is quite close to that of the sample.

In summary, we have shown in this section that the local strain field can be consistently defined at the meso-scale and that the six phases SC, SI, SE, WC, WI, WE deform differently from the sample and from each other. The local strain is essentially governed by the orientation of the phases, in particular for the strongly elongated phases SC, SI, SE.

4. Stress at the meso-scale

The main difficulty when defining a stress field at the meso-scale is that the volume V^h of a meso-domain is different from the volume (denoted as $\widehat{V}^h$) to which the external forces of the meso-domain are applied (forces at the contacts

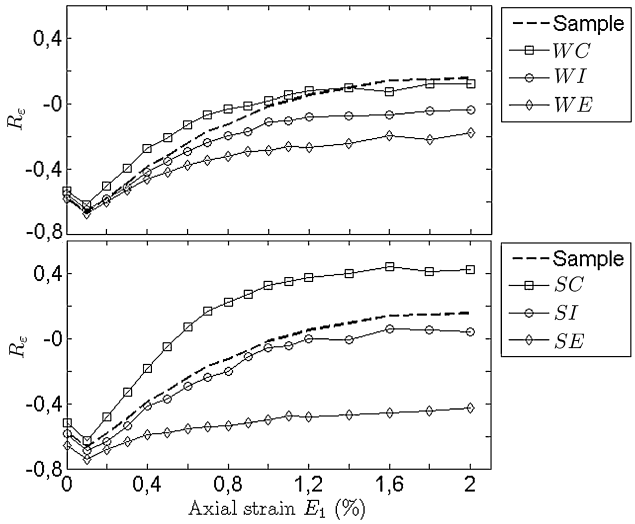

Fig. 13. Evolution of the strain ratio $R_\varepsilon = (\delta\varepsilon_{11} + \delta\varepsilon_{22})/(\delta\varepsilon_{22} - \delta\varepsilon_{11})$ of the six phases during loading.

between the particles of the meso-domain and neighbouring particles in contact), as illustrated in Fig. 14. Volume $\widehat{V}^h$ is obtained by gathering all the Dirichlet cells attached to each particle of the sub-domain under consideration (see [12] for more details about the Dirichlet cell system). In addition, the set of volumes $\widehat{V}^h$ is not additive, i.e. volumes $\widehat{V}^h$ intersect each other. Two definitions have been proposed by Nguyen et al. [18] to overcome this. Each definition has some advantages and some drawbacks as discussed in [18]. In this paper, we present one of these definitions which possesses, in our opinion, a clear physical basis. According to this method, the stress tensor $\boldsymbol{\sigma}^h$ to be defined for a meso-domain with volume V^h is assumed to be equal to the mean stress tensor that is defined over volume $\widehat{V}^h$, despite the fact that volume $\widehat{V}^h$ comprises volume V^h. Fig. 14 illustrates volumes $\widehat{V}^h$ and V^h for a meso-domain. This assumption leads to:

$$\boldsymbol{\sigma}^h = \frac{1}{\widehat{V}^h}\left\{\sum_{c\in K^h_{\text{int}}} \boldsymbol{f}^c \otimes \boldsymbol{l}^c + \sum_{c\in K^h_{\text{ext}}} \boldsymbol{f}^c \otimes \boldsymbol{r}^c\right\} \tag{10}$$

where K^h_{ext} and K^h_{int} are respectively the sets of external and internal contacts of meso-domain h; and $\boldsymbol{l}^c$ and $\boldsymbol{r}^c$ are respectively branch and contact vectors as illustrated in Fig. 15 (see [18] for more details about this definition). Note that the mean stress tensor over volume $\widehat{V}^h$ (the right hand side in (10)) is consistently defined with a strong physical base as discussed in [18]. The weak point in this definition lies in the assumption mentioned above, because of the difference between volumes $\widehat{V}^h$ and V^h. The macroscopic stress $\boldsymbol{\Sigma}$ is estimated as the volume-weighted mean tensor of $\boldsymbol{\sigma}^h$ over all the meso-domains in the sample (volume V^h of each meso-domain is considered as the weight in this average). It has been shown in [18] that the assumption used in this stress definition leads to an overestimation by about 6% of the macroscopic stress defined from the boundary conditions. However, the macroscopic stress ratio Q/P, that is usually considered as an important static variable, is quite well estimated.

The meso-stress field defined above has been analysed in detail in [18]. Like the meso-strain field, the meso-stress field is heterogeneous, as shown in Fig. 16. The stress of meso-domains is significantly dispersed around the macroscopic stress. In the following, we present some brief analyses of the local stress within the six local phases SC, SI, SE, WC, WI, WE. The stress tensor $\boldsymbol{\sigma}$ for each phase is defined as the volume-weighted mean tensor of $\boldsymbol{\sigma}^h$ over all the meso-domains in the phase under consideration. The local stress state of each phase is analysed using a mean stress:

$$p = \frac{\sigma_{11} + \sigma_{22}}{2} \tag{11}$$

and a stress ratio:

$$R_\sigma = \frac{\sigma_{11} - \sigma_{22}}{\sigma_{11} + \sigma_{22}} \tag{12}$$

where σ_{11} and σ_{22} are the stress components of the phase under consideration in the principal directions (1) and (2) of the macroscopic stress, respectively.

Fig. 17 shows the evolution of the mean stress p of the six phases during loading. We can see that the local mean stress p is approximately uniform for all the phases whatever their orientation, and it is quite close to the macroscopic mean stress P.

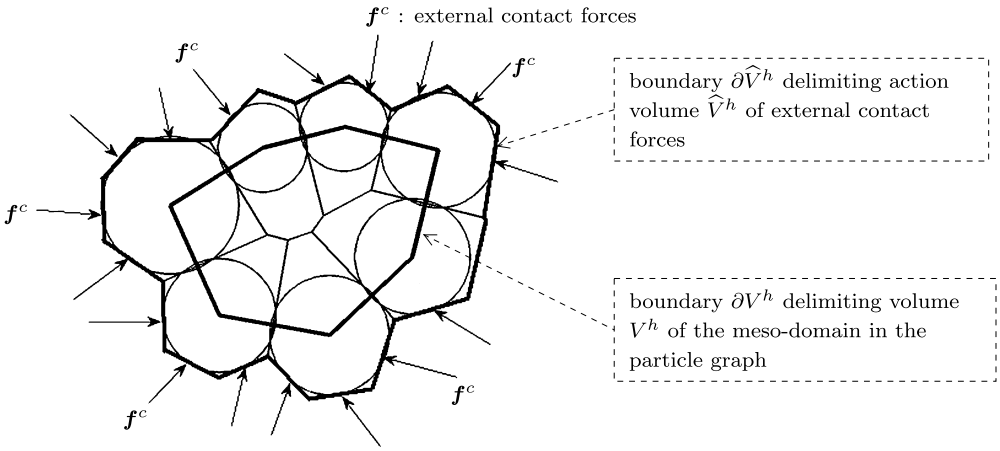

Fig. 14. Illustration of a meso-domain, whose volume in the particle graph is defined by V^h, loaded by the external contact forces applied on an external boundary, $\partial\widehat{V}^h$, delimiting a greater volume, $\widehat{V}^h$. Volume $\widehat{V}^h$ can be defined as the union of Dirichlet cells associated with the particles of the meso-domain [18].

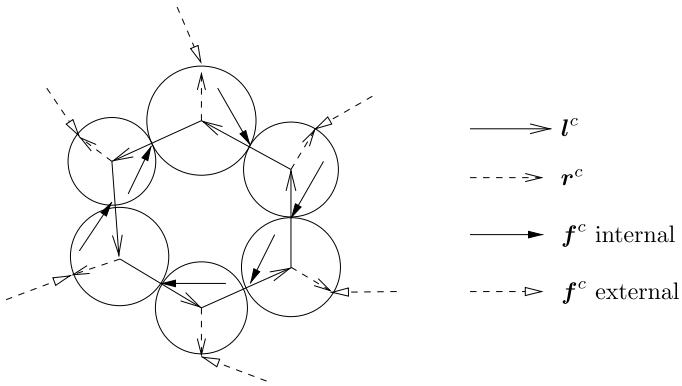

Fig. 15. Set of internal contacts K^h_{int} with branch vector $\boldsymbol{l}^c$ and internal contact force $\boldsymbol{f}^c$; and set of external contacts K^h_{ext} with contact vector $\boldsymbol{r}^c$ and external contact force $\boldsymbol{f}^c$ for a meso-domain.

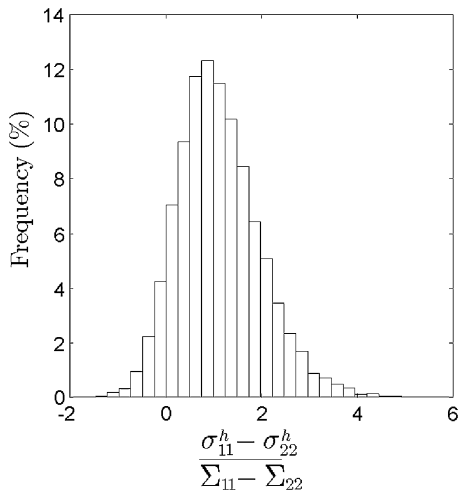

Fig. 16. Distribution of $\sigma^h_{11} - \sigma^h_{22}$ of meso-domains, normalized by $\Sigma_{11} - \Sigma_{22}$, at the loading level $E_1 = 1.2\%$.

Let us now establish the relation between the global stress ratio Q/P defined by Eq. (2) and the local stress ratio R_σ defined by Eq. (12) for the phases considered in this paper. Using the result mentioned above—that the mean stress within each phase is close to the global one, i.e. $(\sigma_{11} + \sigma_{22})/2 \approx P$—we obtain:

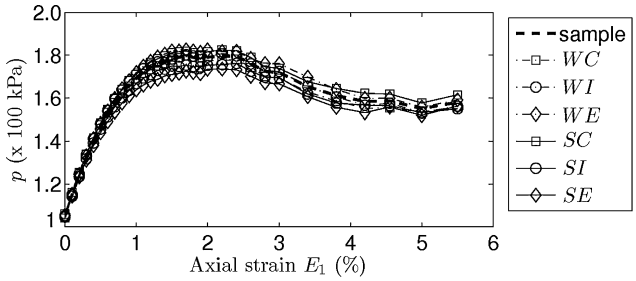

Fig. 17. Evolution of the mean stress p of the six phases during loading, compared to the evolution of the macroscopic mean stress P.

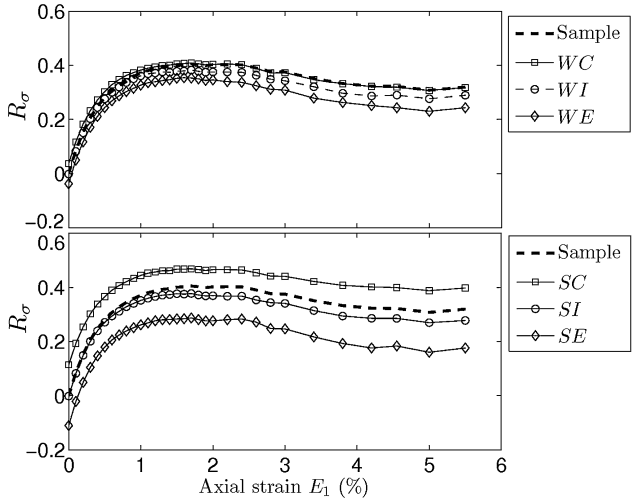

Fig. 18. Evolution of the stress ratio $R_\sigma = (\sigma_{11} - \sigma_{22})/(\sigma_{11} + \sigma_{22})$ of the six phases during loading, compared to the evolution of the global stress ratio Q/P.

$$Q/P = \frac{1}{V}\sum_{i=1}^{6} V^i \frac{\sigma_{11}^i - \sigma_{22}^i}{\sigma_{11}^i + \sigma_{22}^i} = \frac{1}{V}\sum_{i=1}^{6} V^i R_\sigma^i \tag{13}$$

where superscript i depicts each phase among the six phases SC, SI, SE, WC, WI, WE; and V_i and V are respectively the volumes of each phase and of the sample. From Eq. (13), the local stress ratio R_σ can be taken as the contribution of each phase to the global stress ratio Q/P.

Fig. 18 shows the evolution of the stress ratio R_σ of the six local phases during loading. It can be seen that, at the initial state where the macroscopic stress ratio Q/P is equal to zero, the value of R_σ for phase SC is positive, which is opposite to the negative value for phase SE, while the value for phase SI is approximately zero. The negative value of R_σ for phase SE is due to the orientation of this phase in the extension direction (2), leading to a higher value of stress component σ_2 than the value of stress component σ_1 within this phase. During the biaxial test, the local stress ratio R_σ of the six phases increases according to the phase orientation, in particular for the strongly elongated phases. R_σ of phase SE becomes positive when the deviatoric loading is sufficiently high. The value of R_σ for phase SC is higher than stress ratio Q/P of the sample, while the value for phase SE is lower than Q/P. On the other hand, phase SI has a stress ratio R_σ close to the global stress ratio Q/P. These results emphasize the fact that when a granular material is subjected to deviatoric loading, the local phases contribute differently to support the deviatoric loading, depending on their orientation, particularly for the strongly elongated phases. Phase SC oriented in the compression direction supports much more than phase SE oriented in the extension direction, while the contribution of phase SI oriented in the intermediate direction falls between phases SC and SE.

5. Behaviour of the granular material at the meso-scale

In this section, we will analyse the behaviour of the six phases SC, SI, SE, WC, WI, WE defined in Section 2.3.1. The analysis of the behaviour of each phase will focus on some important states during loading such as initial, characteristic, peak and critical states, and on the local stress–strain relation. The stress state is studied through the stress ratio R_σ defined by Eq. (12), and the strain state is studied through the strain ratio R_ε defined by Eq. (9).

Table 2
Values of different parameters of the sample and of the six phases at the initial state.

	Sample	WC	WI	WE	SC	SI	SE
P_V		0.16	0.16	0.17	0.17	0.17	0.17
T_d	0.0	0.14	0.0	−0.14	0.14	0.0	−0.14
po	0.19	0.21	0.21	0.22	0.17	0.17	0.16
r	4.0	3.6	3.6	3.6	4.6	4.6	4.5
R_σ	0.0	0.04	0.0	−0.04	0.11	0.0	−0.11
R_ε	−0.57	−0.53	−0.55	−0.58	−0.52	−0.59	−0.66

Table 3
Values of different parameters of the six phases and of the sample at the characteristic state.

	Sample	WC	WI	WE	SC	SI	SE
E_1	1.1%	1.0%	2.0%	–	0.5%	1.2%	–
P_V		0.15	0.11	–	0.21	0.16	–
T_d	0.19	0.16	0.0	–	0.17	0.01	–
po	0.18	0.22	0.21	–	0.17	0.16	–
r	4.1	3.9	3.8	–	4.7	4.7	–
R_σ	0.38	3.8	0.38	–	0.37	0.37	–

a) Initial state

Table 2 presents some characteristics of the sample and of the six phases at the initial state, such as the amount of volume P_V, the measure of anisotropy $T_d = T_{11} - T_{22}$ with the texture tensor $\boldsymbol{T}$ defined by Eq. (6), porosity po, valence r, the stress ratio R_σ and the strain ratio R_ε. Note that the sample is isotropic and the global stress is also isotropic at the initial state. The isotropy of the sample is reflected by the fact that, on the one hand, the volume of the sample is uniformly partitioned into the six phases, whatever the orientation of the phases, and, on the other hand, the density of the phases (porosity po and valence r) is independent of the phase orientation. Moreover, the positive contributions of phases SC and WC to the global anisotropy are completely counterbalanced by the negative contributions of phases SE, WE. The initial density of the phases depends only on the phase elongation degree: the strongly elongated phases (SC, SI, SE) are denser than the weakly elongated phases (WC, WI, WE), i.e. the former have a lower porosity po and a higher valence r than the latter.

The local stress is not uniform within the phases even at the initial state, in particular within the strongly elongated phases, which is demonstrated by the dependence of the local stress ratio R_σ on phase orientation. The global isotropic stress is reflected by the fact that the positive values of R_σ for phases SC and WC are opposite to the negative values for phases SE and WE. The negative values of the local strain ratio R_ε show that all the phases are contracting at the initial state. In particular, phase SE oriented in the extension direction contracts much more than phase SC oriented in the compression direction ($R_\varepsilon = -0.66$ for phase SE compared to $R_\varepsilon = -0.52$ for phase SC).

b) Characteristic state

The characteristic state of a phase is defined as the state at which the phase under consideration changes from contractive to dilative behaviour (thus, strain ratio R_ε is zero at this state). Table 3 encapsulates some parameters of the phases and of the sample at the respective characteristic states. We can see in Fig. 13 and in Table 3 that the six phases reach the characteristic state differently from the sample, and from each other. The phases oriented in the compression direction (SC, WC) reach this state before the sample, whereas the phases oriented in the extension direction (SE, WE) have not yet reached the characteristic state in the studied range of loading. One can remark that the local density at the characteristic state is practically independent of the phase orientation.

As shown in Table 3, the values of R_σ at the characteristic state for phases SC, WC, SE, WE are quite close to each other, and they are also close to the corresponding value of the sample ($R_\sigma \approx 0.38$). In addition, the stress ratio R_σ of phases SE and WE, which have not yet reached the characteristic state, is lower than the value 0.38 mentioned above (Fig. 18).

c) Peak state

The peak state of a phase is the state at which the stress ratio R_σ within the considered phase is maximum. Table 4 presents some characteristics of the six phases and of the sample at the peak state. We can see in Fig. 18 and in Table 4 that all the six phases reach the peak state at approximately the same axial strain E_1 of 2%, at which the sample also reaches the peak state. At this state, the volume of phase SC reaches approximately the maximum value, while the volume of phase SE reaches the minimum value as shown in Fig. 7. As a consequence, phase SC contributes mainly to the global anisotropy

Table 4
Values of different parameters of the sample and of the six phases at the peak state.

	Sample	WC	WI	WE	SC	SI	SE
E_1	2.0%	2.0%	2.0%	2.0%	2.0%	2.0%	2.0%
P_V		0.20	0.13	0.11	0.35	0.14	0.07
T_d	0.33	0.17	0.0	−0.09	0.30	0.01	−0.06
po	0.19	0.24	0.21	0.18	0.19	0.17	0.16
r	4.4	4.1	3.8	3.6	5.3	4.8	4.4
R_σ	0.40	0.40	0.38	0.35	0.47	0.37	0.28
R_ε	0.15	0.12	−0.04	−0.18	0.42	0.04	−0.43

Table 5
Values of different parameters of the sample and of the six phases at the critical state.

	Sample	WC	WI	WE	SC	SI	SE
E_1	7.0%	5.0%	5.0%	5.0%	5.0%	5.0%	5.0%
P_V		0.19	0.13	0.11	0.35	0.15	0.07
T_d	0.33	0.17	0.0	−0.09	0.29	0.01	−0.05
po	0.21	0.25	0.22	0.21	0.20	0.18	0.17
r	4.5	4.2	4.0	3.8	5.3	5.0	4.6
R_σ	0.31	0.31	0.28	0.23	0.39	0.27	0.16

($T_d^{SC} = 0.33$), while the role of phase SE in reducing the anisotropy created by phase SC is not important ($T_d^{SE} = -0.06$). Moreover, the difference in the density between the phases is great at the peak state: phase SC (resp. WC) is much looser than phase SE (resp. WE).

We can see that the local stress ratio R_σ of the phases is highly governed by phase orientation at the peak state, in particular for the strongly elongated phases: R_σ of phase SC is much higher than R_σ of phase SE. Another point is that the local strain ratio R_ε of the phases depends highly on phase orientation at this state. Phase SC presents a high dilatancy ($R_\varepsilon = 0.42$ compared to a value of 0.15 for the sample), whereas phase SE is still contracting considerably ($R_\varepsilon = -0.43$). In fact, the dilatancy of a granular material has been shown to be maximum at the peak state in many studies, in particular in [25,26]. In the case of the six local phases considered in the present paper, we can observe that the local strain ratio R_ε of each phase remains approximately constant near the peak state and seems to reach the maximum value at this state. However, this observation should be confirmed in more detailed analyses, in which the evolution of the local strain after the peak state can be studied with a suitable method which takes into account the formation of shear bands inside the sample.

d) Critical state

This state is the final state of a granular material under deviatoric loading, where the material evolves without any volume change. Moreover, the stress ratio remains constant at this state. It can be seen in Figs. 8, 10 and 18 that the anisotropy measure T_d, the valence r and the stress ratio R_σ for all the phases remain approximately constant at the axial strain $E_1 = 5\%$. However, the local porosity po of the phases is not yet completely constant at this level of the axial strain as the sample continues to dilate slightly until $E_1 = 7\%$. We consider roughly that all the phases reach the critical state at $E_1 = 5\%$. Some characteristics of the phases and of the sample are shown in Table 5. We can see that the amount of volume P_V and contribution T_d of the phases to the global anisotropy are close to the respective values at the peak state shown in Table 4. Nevertheless, the phases at this state have a higher porosity and a higher valence than at the peak state. This is similar to what is observed for the sample, for which the porosity po and the coordination number $\overline{N}$ related to mean valence R are highest at the critical state (Figs. 9 and 10). The local stress ratio R_σ of the phases at this state are significantly lower than the respective values at the peak state. One can remark that the local density and local stress ratio R_σ of the phases are still dependent on the phase orientation at the critical state.

e) Stress–strain relation

In the following, we will investigate how the strain and stress states within the local phases are related to each other. Firstly, we can observe in Figs. 13 and 18 that the strongly elongated phases present remarkably different behaviours during loading, depending on the phase orientation. Phase SC oriented in the compression direction presents the typical behaviour of a dense granular material with a high stress ratio and high dilatancy, whereas phase SE oriented in the extension direction presents the typical behaviour of a loose material with a low stress ratio and high contractancy. Phase SI with the intermediate orientation between the compression and extension directions presents the behaviour of a material with an intermediate density. It is interesting to note that phase SC is looser than phase SE (Fig. 9); however, the former behaves like a dense granular material, whereas the latter behaves like a loose material. This shows that the behaviour of the phases

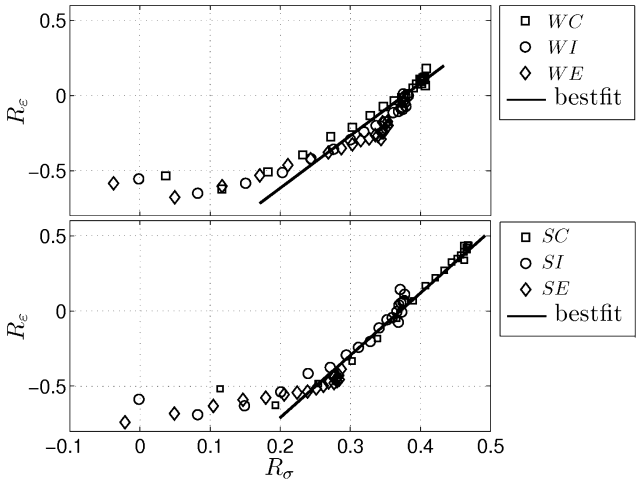

Fig. 19. Local strain ratio R_ε versus local stress ratio R_σ for the phases SC, SI, SE, WC, WI, WE.

is essentially driven by phase texture, not by phase density. As a consequence, when analysing and modelling the local behaviour at the meso-scale, one should focus rather on local texture than on local density.

In order to analyse more clearly the relation between local stress and strain within the phases, in Fig. 19 we plot local strain ratio R_ε versus local stress ratio R_σ for all the phases. The set of points for each phase shown in the figure corresponds to different levels of loading up to the axial strain $E_1 = 2\%$. We can see that, on the whole, local strain ratio R_ε increases with local stress ratio R_σ for any phase, in particular when local stress ratio R_σ is sufficiently high (when $R_\sigma > 0.2$). A slight dependence is observed for $R_\sigma \leqslant 0.2$, which may be due to the fact that the contractive behaviour of the phases is governed by local isotropic stress that dominates local deviatoric stress. One can remark that local strain ratio R_ε increases more or less linearly with local stress ratio R_σ when $R_\sigma > 0.2$ whatever the phase orientation. In particular, the slope of the R_ε–R_σ relation for the strongly elongated phases (SC, SI, SE) is quite close to that for the weakly elongated phases (WC, WI, WE).

Many studies in the literature have emphasized the relation between stress ratio and strain ratio in a granular material [25–28]. This relation is usually called the "stress–dilatancy relation". When a material is subjected to deviatoric loading, it tends to dilate in order to resist the loading, so the resistance of the material depends on how much it is able to dilate. We have observed that the considered local phases present a similar behaviour. Phase SC is able to dilate widely (because it is oriented in the compression direction), so it can withstand a high stress ratio. On the other hand, phase SE is not able to dilate (because it is oriented in the extension direction) so it can only withstand a low stress ratio. The stress–dilatancy relation for a granular material has been shown to be approximately linear. This linear stress–dilatancy relation has been theoretically formulated by Rowe [28] and experimentally confirmed by many authors, in particular by Bolton [27]. The above result shows that the local phases considered in the present paper follow Rowe's stress–dilatancy relation closely well, whatever the phase elongation degree and orientation.

f) Relation between the behaviour of the granular material at the RVE scale and at the meso-scale

In the previous paragraphs, we have analysed the local behaviour of the granular sample considered in this paper at the meso-scale. Considering this local scale, the sample can be thought to be composed of meso-domains which are loops enclosed by particles in contact. It has been shown that the texture of meso-domains is very heterogeneous, with different elongation degrees and orientations. In this paper, for the sake of simplicity, we have chosen to classify all the meso-domains in the sample into six phases which differ from each other in their elongation degree (strongly and weakly elongated) and in their orientation (in the compression, intermediate and extension directions). Of course, this classification is not the only possible one. Each phase occupies a certain volume in the sample and represents a distinct local structure of the sample. The evolution of the internal state of the sample during loading is described by the evolution in volume of the local phases, which is governed by the texture of each phase. The behaviours of the local phases are different from each other, and depend on the texture of each phase. Thus, the behaviour of each phase can be considered as an intrinsic property depending only on the texture of the considered phase. The behaviour of the sample during loading has been shown to be the average behaviour of the local phases. Consequently, in order to define the behaviour of a granular material at the representative elementary volume (RVE) from the local behaviour of the material at the meso-scale using a multi-scale approach, it would be necessary:

- to define the behaviour of each local phase according to its texture characteristic and on the principal directions of loading;

- to define the evolution in volume of each local phase, according to its texture characteristic;
- to consider a volume average of different state variables (stress, strain, texture) over all the local phases to obtain the behaviour at the RVE scale.

6. Conclusions

The local behaviour of a 2D granular material at the so-called meso-scale has been analysed in this paper. At this scale, a granular material is considered to be composed of meso-domains which are loops enclosed by particles in contact. Texture characteristics (elongation degree and orientation), stress and strain tensors at the meso-scale have been defined. The analyses carried out on a numerical granular sample subjected to a biaxial compression test have shown that the local strain and stress fields present a structured nature at the meso-scale. In this paper, six local phases have been defined on the basis of meso-texture characteristics. Each phase is a set of meso-domains with similar elongation degrees and similar orientations. These local phases have been shown to evolve differently and have distinct behaviours, depending on their texture characteristics. In particular:

- at the initial state where the sample and the stress state are isotropic, the major principal direction of the local deviatoric stress is coincident with the elongation direction of the local texture;
- the phases oriented in the compression direction of the biaxial loading test show a remarkably higher value of the stress at the peak state than the phases oriented in the extension direction;
- the dilatancy of the phases oriented in the compression direction is much higher than that of the phases oriented in the extension direction;
- the phases oriented in the compression direction behave like a dense material, while the phases oriented in the extension direction behave like a loose material;
- a stress–dilatancy relationship seems to exist at the meso-scale and seems to be independent of the elongation degree and orientation of the local phases;
- the global behaviour of the sample can be considered as being an average of that of the local phases.

The analyses presented in this paper bring more information on local phenomena occurring in granular materials and more understanding of the complex behaviour of this kind of materials. As a result, the constitutive modelling of granular materials might be improved with a multi-scale approach based on the defined meso-scale. Such an approach should take into account local phenomena observed at this scale. This constitutes the subject of our future work.

References

[1] K. Walton, The effective moduli of a random packing of spheres, J. Mech. Phys. Solids 3 (35) (1987) 213–226.
[2] F. Emeriault, B. Cambou, Micromechanical modelling of anisotropic non-linear elasticity of granular medium, Int. J. Solids Struct. 33 (18) (1996) 2591–2607.
[3] K. Sab, Une nouvelle approche de l'homogénéisation des milieux granulaires, in: Saint-Venant Symposium: Analyse multiéchelle et systèmes physiques couplés, Presses de l'École nationale des ponts et chausées, Paris, 1997.
[4] C.L. Liao, T.P. Chang, D.H. Young, C.S. Chang, Stress–strain relationships for granular materials based on the hypothesis of best-fit, Int. J. Solids Struct. 34 (1997) 4087–4100.
[5] I. Goldhirsch, C. Goldenberg, On the microscopic foundations of elasticity, Eur. Phys. J. E 9 (2002) 245–251.
[6] C.S. Chang, P.-H. Hicher, An elasto-plastic model for granular materials with microstructural consideration, Int. J. Solids Struct. 42 (14) (2005) 4258–4277.
[7] C.S. Chang, A. Misra, Application of uniform strain theory to heterogeneous granular solids, J. Eng. Mech. 116 (10) (1990) 2310–2328.
[8] B. Cambou, P. Dubujet, F. Emeriault, F. Sidoroff, Homogenization for granular materials, Eur. J. Mech. A, Solids 14 (2) (1995) 255–276.
[9] F. Emeriault, C.S. Chang, Interparticle forces and displacements in granular materials, Comput. Geotech. 20 (3/4) (1997) 223–244.
[10] B. Cambou, M. Chaze, F. Dedecker, Change of scale in granular materials, Eur. J. Mech. A, Solids 19 (6) (2000) 999–1014.
[11] K. Bagi, Analysis of microstructural strain tensors for granular assemblies, Int. J. Solids Struct. 43 (2006) 3166–3184.
[12] M. Satake, A discrete-mechanical approach to granular materials, Int. J. Eng. Sci. 30 (10) (1992) 1525–1533.
[13] N. Kruyt, L. Rothenburg, Micromechanical definition of the strain tensor for granular materials, J. Appl. Mech. 118 (1996) 706–711.
[14] M.R. Kuhn, Deformation measures for granular materials, in: Mechanics of Deformation and Flow of Particulate Materials, ASCE, 1997, pp. 91–104.
[15] O. Durán, N.P. Kruyt, S. Luding, Analysis of three-dimensional micro-mechanical strain formulations for granular materials: evaluation of accuracy, Int. J. Solids Struct. 47 (2010) 251–260.
[16] O. Durán, N.P. Kruyt, S. Luding, Micro-mechanical analysis of deformation characteristics of three-dimensional granular materials, Int. J. Solids Struct. 47 (2010) 2234–2245.
[17] N.S. Nguyen, H. Magoariec, B. Cambou, A. Danescu, Analysis of structure and strain at the meso-scale in 2D granular materials, Int. J. Solids Struct. 46 (2009) 3257–3271.
[18] N.S. Nguyen, H. Magoariec, B. Cambou, Local stress analysis in granular materials at a meso-scale, Int. J. Numer. Anal. Methods Geomech. 36 (14) (2011) 1609–1635.
[19] P.A. Cundall, A computer model for simulating progressive large scale movements in blocky rock systems, in: Proceedings of the Symposium of the International Society of Rock Mechanics, Nancy, France, 1971, 1(II-8).
[20] Itasca Consulting Group, Inc., PFC2D – Theory and Background, 1999.
[21] T. Tsuchikura, M. Satake, Statistical measure tensors and their application to computer simulation analysis of biaxial compression test, in: H. Murakami, J.E. Luco (Eds.), Engineering Mechanics: A Force for 21st Century, ASCE, Reston, VA, 1998, pp. 1732–1735.
[22] M.R. Kuhn, Structured deformation in granular materials, Mech. Mater. 31 (1999) 407–429.
[23] Z.P. Bazant, J. Ozbolt, Non local microplane model for fracture, damage, and size effects in structures, J. Eng. Mech. 116 (11) (1990) 2485–2505.

[24] K. Bagi, Stress and strain in granular assemblies, Mech. Mater. 22 (1996) 165–177.
[25] A. Casagrande, Characteristics of cohesionless soils affecting the stability of slopes and earth fills, in: Contribution to Soil Mechanics 1925–1940, Boston Society of Civil Engineering, 1940, pp. 257–276.
[26] D.W. Taylor, Fundamentals of Soil Mechanics, John Wiley & Sons, 1948.
[27] M.D. Bolton, The strength and dilatancy of sands, Geotechnique 36 (1) (1986) 65–78.
[28] P.W. Rowe, The stress–dilatancy relation for static equilibrium of an assembly of particles in contact, Proc. R. Soc. A, Math. Phys. Eng. Sci. 269 (1962) 500–572.